Revisiting the phase diagram and piezoelectricity of lead zirconate titanate from first principles

Yubai Shi [1,2] Ri He [1,*] Bingwen Zhang,[3] and Zhicheng Zhong [1,4,†]

[1]*CAS Key Laboratory of Magnetic Materials, Devices and Zhejiang Province Key Laboratory of Magnetic Materials and Application Technology, Ningbo Institute of Materials Technology and Engineering, Chinese Academy of Sciences, Ningbo 315201, China*

[2]*College of Materials Science and Opto-Electronic Technology, University of Chinese Academy of Sciences, Beijing 100049, China*

[3]*Fujian Key Laboratory of Functional Marine Sensing Materials, Center for Advanced Marine Materials and Smart Sensors, College of Material and Chemical Engineering, Minjiang University, Fuzhou 350108, China*

[4]*China Center of Materials Science and Optoelectronics Engineering, University of Chinese Academy of Sciences, Beijing 100049, China*

Lead zirconate titanate (PbZr$_{1-x}$Ti$_x$O$_3$, PZT) exhibits excellent piezoelectric properties in the morphotropic phase boundary (MPB) region of its temperature-composition phase diagram. However, the microscopic origin of its high piezoelectric response remains controversial. Here, we develop a machine-learning-based deep potential (DP) model of PZT using the training data set from first-principles density functional theory calculations. Based on DP-assisted large-scale atomic simulations, we reproduce the temperature-composition phase diagram of PZT, in good agreement with the experiment except for the absence of structural transition from *R3c* to *R3m*. We find that the rhombohedral phase maintains *R3c* symmetry with slight oxygen octahedral tilting with increase of temperature, instead of exhibiting *R3m* symmetry. This discrepancy could trace back to the lack of experimental measurements to identify such slight octahedral tilting. More importantly, we clarify the atomic-level feature of PZT at the MPB, which exhibits the competing coupling of ferroelectric nanodomains with various polarization orientations. The high piezoelectric response is driven by the polarization rotation of nanodomains induced by an external electric field.

I. INTRODUCTION

Lead zirconate titanate (PbZr$_{1-x}$Ti$_x$O$_3$, PZT) is of great interest due to its excellent piezoelectric response. PZT possesses the typical *AB*O$_3$ perovskite structure, where oxygen atoms form octahedra, Pb atoms occupy the interstices of the octahedra, and Zr and Ti atoms reside at the center of the octahedra with disordered distribution. Thus, the solid solution structure leads to a complex temperature-composition phase diagram (see Fig. 1) [1,2]. PZT presents a paraelectric cubic phase at high temperature. When the temperature decreases, an antiferroelectric orthorhombic phase appears near the pure PbZrO$_3$ (PZO). As the concentration of Ti increases, the region enriched in Zr forms a ferroelectric rhombohedral phase with polarization along the ⟨111⟩ orientation, while the Ti-enriched area adopts a ferroelectric tetragonal phase with polarization along the ⟨001⟩ orientation. In particular, the nearly vertical phase boundary between the tetragonal and rhombohedral regions close to $x = 0.5$, called the morphotropic phase boundary (MPB), exhibits fascinating physical properties [3,4].

Although it is well known that the high piezoelectricity of PZT is related to the MPB, the exact microscopic origins are still unclear [5]. The MPB solid solution presents complex multidomain structures, featuring the coexistence and coupling competition of multiple phases. Therefore, the study of its properties is rather complicated. Various theories have been proposed to explain the origins of high piezoelectricity at the MPB. For example, Isupov *et al.* believed the mechanism resulting in enhanced properties was due to the coexistence of tetragonal and rhombohedral phases in the vicinity of the MPB and Kakegawa *et al.* confirmed the coexistence of these phases by experiments [6–11]. Furthermore, Fu *et al.* suggested that a large piezoelectric response was driven by polarization rotation induced by an external field [12–15], whereas Frantti *et al.* proposed that the phase instability, in contrast to the polarization rotation, was responsible for the large piezoelectric properties observed in PZT near the MPB [16–19]. In addition, Li *et al.* found that local fluctuations of a polarization vector might result in a unique domain structure, such as nanometer ferroelectric domains, which could be the crucial factor responsible for the excellent piezoelectric response in PZT [20–24]. More recently, Yan *et al.* believed that an oxygen octahedral tilting-untilting transition at the *R3c/P4mm* MPB leads to a high free-energy barrier and results in low piezoelectric activity, whereas the *R3m/P4mm* MPB with octahedral untilting produces large piezoelectricity due to the low free-energy barrier at such an MPB [25]. Due to the experimental challenges in characterizing the composition distribution and complex microscopic structures at the MPB, resolving these controversies is rather difficult.

Atomic simulation from first principles is an effective method for studying such complex solid solutions and its thermodynamics properties. Regrettably, the structural thermodynamics properties of these complex systems prove to be beyond the capacity of density functional theory (DFT)

---

*heri@nimte.ac.cn

†zhong@nimte.ac.cn
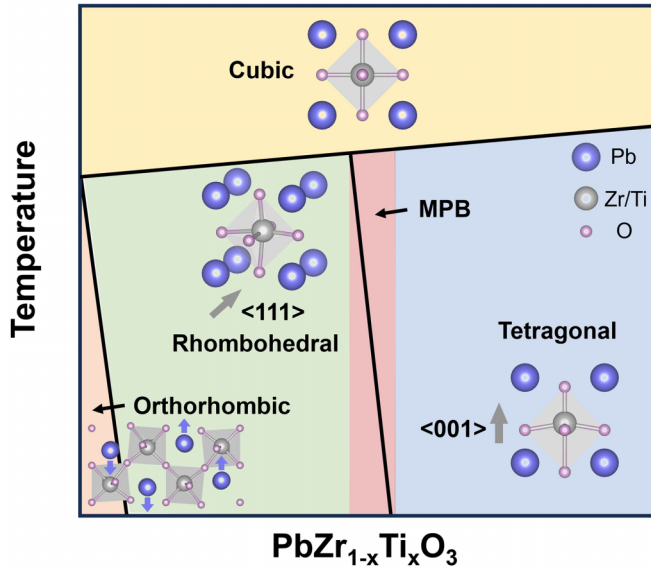
FIG. 1. A simple schematic diagram includes the temperature-composition phase diagram of PZT and structural characteristics of each phase.

FIG. 2. The workflow of the DP model generation for $PbZr_xTi_{1-x}O_3$. Iterative training with different components individually, including $x = 0$, 0.125, 0.25, 0.5, 0.75, 0.875, and 1. After convergence of each component, the data sets with different x are collected into the final data set. A DP model was generated through a long-step training based on this final training data set.

due to the large system sizes and simulation times involved. To solve this issue, we utilize a machine-learning-based deep potential (DP) model to perform large-scale atomic simulation. Machine-learning potentials use a deep neural network to capture the potential energy surface of a material system in DFT accuracy. Recent research utilizing the DP method has witnessed numerous breakthroughs in the field of ferroelectric perovskite materials [26–29], providing compelling evidence for the reliability of this technique.

Herein, we develop a machine-learning-based potential for PZT using a data set from DFT calculations. The DP model can effectively reproduce the temperature-composition phase diagram and properties of PZT. Importantly, DP-predicted results reveal the absence of the *R3m* structure, which was claimed to be observed in experiment. We attribute this discrepancy to limitations in experimental measurements. We calculated the piezoelectric constant (d_{33}) over a whole range of compositions, demonstrating the highest piezoelectric response of the MPB region compared to other components. Furthermore, we reveal that the mechanism underlying the ultrahigh piezoelectric response of the MPB is driven by polarization rotation. Our work clarifies the origin of high piezoelectricity at the MPB in PZT from the atomic level, paving the way for the experimental design of novel piezoelectric materials.

II. COMPUTATIONAL METHODS

A. Generation of the DP model

The selection of the training data sets is crucial for the accuracy of the DP model. This requires the training data sets to comprehensively cover the potential energy surface of the system. Generating configurations for the training set is not a trivial task. Here, we utilize DP-GEN to generate training data sets encompassing a sufficiently broad space of relevant configurations [30]. DP-GEN has been widely utilized over the

past years, and a DP model for variation in material systems has been developed by this strategy [31]. Here, we emphasize only a few key points of the training process. DP-GEN is a concurrent learning procedure, and the workflow of each iteration includes three main steps: training, exploration, and labeling (see Fig. 2). Considering that we aim to describe properties of $PbZr_xTi_{1-x}O_3$ with continuous variations of x, the training data sets include different x values: 0, 0.125, 0.25, 0.5, 0.75, 0.875, and 1. When describing the properties of a system as it varies with temperature, it is necessary to consider different initial structures at different temperatures. For example, when $x = 0$, there are both the $Pm\bar{3}m$ cubic phase, which is stable at high temperatures, and the $Pbam$ orthorhombic phase, which is stable at low temperatures. The configurations of the initial data sets are generated by perturbing the atomic coordinates of these structures. Starting with the above data sets, including configurations and corresponding DFT-calculated energies, four different DP models are trained using the deep potential molecular dynamics (DPMD) method [32], based on different values of deep neural network parameters. The exploration step is performed in which one of the DP models is used for molecular dynamics (MD) simulations at given pressure and temperature to explore the configuration space. We established an extensive exploration range spanning from 50 to 1000 K and from -100 to 10^5 Pa. For all sampled configurations in MD trajectories, the other three DP models will predict the atomic forces of all atoms. The maximum standard deviation of atomic forces F_i is used to construct an error indicator for labeling: $\sigma_f^{max} = \max \sqrt{\langle |F_i - \langle F_i \rangle|^2 \rangle}$, where $\langle \cdots \rangle$ indicates the average of the DP-predicted force,

and F_i denotes the predicted force on the atom i. When $\sigma_f^{\max} > \sigma_{\text{high}}$, the corresponding configuration is labeled as a failure. Only configurations with $\sigma_{\text{low}} < \sigma_f^{\max} < \sigma_{\text{high}}$ undergo DFT calculations, then get added to the next iteration's training data set. Here, the exploration of each system is considered converged when the percentage of accurate configurations ($\sigma_{\text{low}} < \sigma_f^{\max}$) is $> 99\%$. It is worth noting that all systems are not iterated together. Instead, systems with different x values are individually iterated to ensure each reaches the convergence accuracy. The DP-GEN process stops when all systems have satisfactorily converged. Finally, all data sets are collected and combined into the final training data set for a long-step training. This approach offers the advantage of improving efficiency. What is more, the DP model trained in this way can describe the properties of PZT in continuous variations of x values, and it possesses the same level of accuracy as individually training for a particular x value. We also utilize the compressed model in this work. This method has been proven to significantly enhance the computational efficiency of DPMD, with negligible loss in accuracy [33]. Long-range electrostatic interactions play an important role in dielectric materials simulation. Introducing a cutoff radius limits the interaction range and may potentially overlook certain long-range effects. Nevertheless, in many cases, the finite-range model indeed gives an accuracy of ~ 1 meV/atom in energy, which is comparable with the intrinsic error of the functional approximation adopted in DFT [27,34–36]. This level of accuracy is sufficient for most physical properties of practical interest. Furthermore, a recent method proves that the DP model is capable of accurately describing long-range electrostatic interactions [37]. Thus, it will be possible to simulate piezoelectric materials with long-range electrostatic interactions using the DP model in the future.

B. DFT calculations

The quality of the initial data sets determines the accuracy of the ultimately trained DP model. The initial data sets required for training a deep neural network are entirely generated by the Vienna *Ab initio* Simulation Package (VASP) [38,39], which maintains the precision of first principles. All DFT calculations are performed using a plane-wave basis set with a cutoff energy of 600 eV, and the exchange-correlation energy of electrons is described in the generalized gradient approximation using the PBEsol functional [40]. The Brillouin zone is sampled using k points with a minimum spacing of 0.2 Å^{-1}, including the gamma point. The calculation of the phonon spectrum was carried out using the PHONOPY package [41,42], and the force constant matrix was generated using the finite displacement method, with a $2 \times 2 \times 2$ supercell. Additionally, we introduce the nonanalytic correction (NAC) when performing calculations for the cubic structure to remove the degeneracy of longitudinal optical and transverse optical branches.

C. MD simulations

MD simulations are performed using the LAMMPS code with periodic boundary conditions and at standard pressure to model the temperature and composition-driven structural

transition of PZT [43,44]. Preliminary simulations are with the $10 \times 10 \times 10$ supercell (5000 atoms). While near the key points, such as T_c, the MPB region, and especially the rhombohedral phase region, simulations are extended to a $20 \times 20 \times 20$ supercell (40 000 atoms) as a duplicate verification, which can give similar results. MD simulations adopt the isobaric-isothermal (*NPT*) ensemble with temperature set from 100 to 700 K. The time step is set to 0.001 ps. At a specified temperature, the equilibrium run is 40 ps. The simulation is run for 100 ps near the phase transition point to ensure an adequate amount of statistical data. The simulation environment is set as a triclinic box, allowing for full relaxation of lattice constants and lattice angles. In PZT solid solution, Zr and Ti exhibit a disorder arrangement. Our tests indicate that different disorder configurations have a negligible impact on energy with 0.03 meV/f.u. Applying an electric field to the system is achieved by applying an external force to the atoms as an equivalent method. The forces acting on different atoms are determined by multiplying the electric field by the reference Born effective charge [45]: $Z_{\text{Pb}}^* = 3.90$, $Z_{\text{Zr}}^* = 5.85$, and $Z_{\text{Ti}}^* = 7.06$. Taking into account the solid solution characteristics of PZT, a dynamic average adjustment scheme is applied to the Born effective charge of oxygen atoms: $Z_O^* = -[Z_{\text{Pb}}^* + xZ_{\text{Ti}}^* + (1-x)Z_{\text{Zr}}^*]/3$, where x represents the concentration of Ti. The piezoelectric coefficient d_{33} is obtained based on $d_{33} = (\partial x_3 / \partial E_3)_X$, where E_3 is the external electric field, x_3 the strain induced, 3 the direction along the z axis, and X represents the external stress. The polarization orientation diagram is based on the quasi-two-dimensional structure of a $100 \times 100 \times 2$ supercell obtained after high-temperature annealing at 700 K.

D. Gibbs free energy calculations

Gibbs free energy is a crucial thermodynamic quantity used to assess the stability of phases. In this work, we calculate the free energy of PbZr$_{0.75}$Ti$_{0.25}$O$_3$ in *R3c* and *R3m* symmetries to verify structure stability. Gibbs free energy includes internal energy (U), the contribution of volume (V) expansion, and the contribution of entropy (S). It can be given by the following equation:

$$G = U + PV - TS. \tag{1}$$

The internal energy can be divided into total energy (U_0) and a function of temperature:

$$U = U_0 + U(T). \tag{2}$$

The total energy can be obtained from DFT calculations at 0 K. The internal energy as a function of temperature can be obtained from the density of states of phonons:

$$U(T) = \sum_{v\boldsymbol{q}} \hbar\omega(v\boldsymbol{q})\left[\frac{1}{2} + \frac{1}{e^{\hbar\omega(v\boldsymbol{q})/k_B T} - 1}\right]. \tag{3}$$

Heat capacity (C_V) can be expressed as

$$C_V(T) = \frac{\partial U(T)}{\partial T}. \tag{4}$$

The entropy is composed of vibrational entropy (S_{phonon}), configurational entropy (S_{conf}), and the contribution of
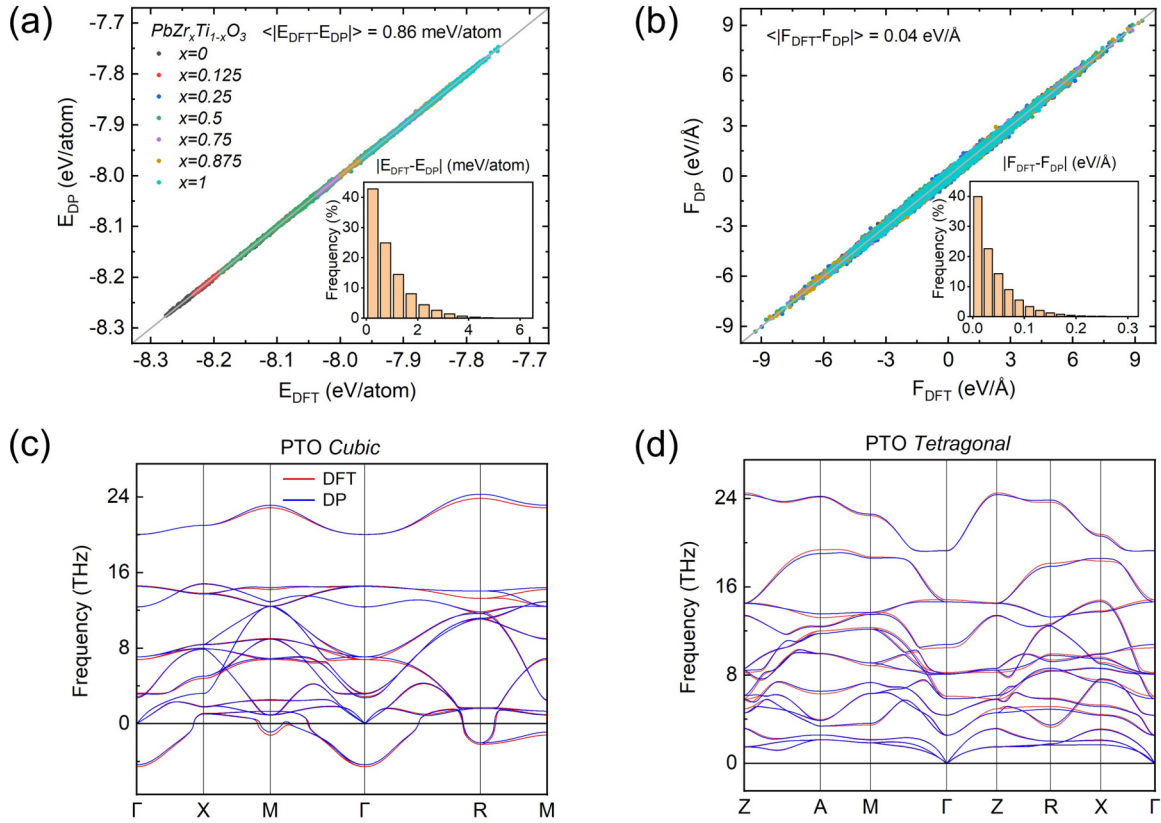
FIG. 3. The comparative analysis involves assessing (a) total energies and (b) atomic forces of PZT with different x values, employing both the DP predictions and DFT calculations. Phonon spectrum of (c) tetragonal PTO and (d) cubic PTO.

electrons (S_{elec}):

$$S = S_{phonon} + S_{conf} + S_{elec}. \tag{5}$$

Here, the contribution from electrons is neglected. Assuming S_{phonon} at 0 K is zero, S_{phonon} is given by

$$S_{phonon} = \int_0^T \frac{C_V(T)}{T} dT. \tag{6}$$

In this work, the configurational entropy is caused by the disorder distribution of B-site atoms, and S_{conf} is given by the analytic equation

$$S_{conf} = -Nk_B[x\ln x + (1-x)\ln(1-x)], \tag{7}$$

where x represents the concentration of Ti and N the total number of B-site atoms.

At last, we neglect the contribution of volume expansion in condensed matter:

$$G = U - T\left\{\left[\int_0^T \frac{C_V(T)}{T} dT - Nk_B[x\ln x + (1-x)\ln(1-x)]\right]\right\}. \tag{8}$$

III. RESULTS AND DISCUSSIONS

A. Accuracy of the DP model

Evaluating the accuracy of the DP model is essential to ensure the reliability of the DPMD simulation results. We compare the energies and atomic forces calculated using the

DP model and DFT calculations for all configurations in the final training data set. As shown in Figs. 3(a) and 3(b), the mean absolute errors of energy ($\Delta E = |E_{DFT} - E_{DP}|$) and atomic force ($\Delta F = |F_{DFT} - F_{DP}|$) between DP and DFT are 0.86 meV/atom and 0.04 eV/Å, respectively. It is evident that the DP model well reproduces DFT results of PZT in different components. These demonstrate the superior representability and flexibility of the DP model in that a single DP model can describe the high-dimensional energy function of complex solid solutions composed of different components of two materials. Because the force constant represents the second derivative of energy with respect to atomic displacement, it serves as a stricter criterion for testing the accuracy of the DP model. Therefore, we employ the DP model and DFT calculations to determine the phonon dispersion relations of PbTiO$_3$ (PTO). As shown in Fig. 3(c), the phonon dispersion of cubic PTO calculated using the DP model agrees well with the DFT result. It is clear that imaginary frequencies appear at the R and Γ points, indicating the cubic phase has multiple lattice instability at 0 K. For the tetragonal phase, the DP model correctly predicted its dynamically stable vibrational modes over the whole Brillouin zone [see Fig. 3(d)]. These results demonstrate that the DP model can effectively describe the characteristics of the interaction between atoms.

B. Phase diagram of PZT solid solutions

In the temperature-composition phase diagram of PZT, there exist both compositional disorder and coupling
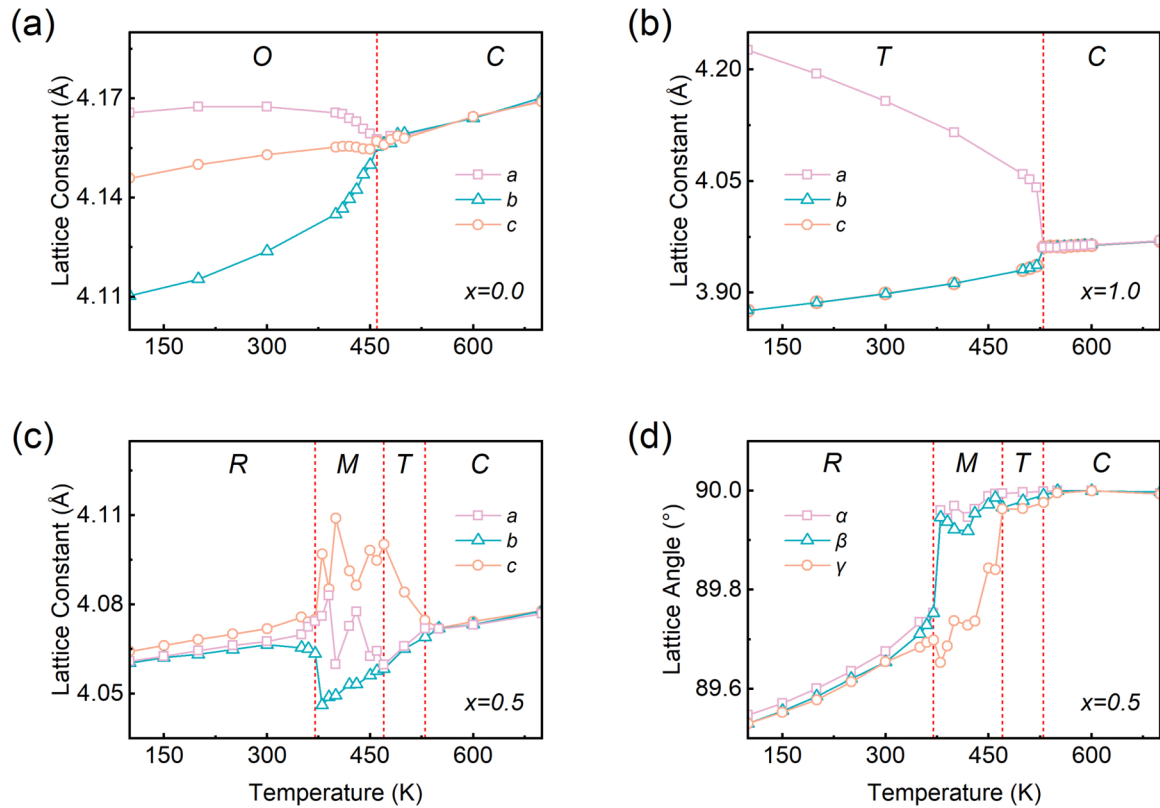
FIG. 4. Schematic representation of the temperature-dependent lattice constants for (a) PbZrO$_3$, (b) PbTiO$_3$, (c) PbZr$_{0.5}$Ti$_{0.5}$O$_3$, and (d) lattice angles for PbZr$_{0.5}$Ti$_{0.5}$O$_3$. O, R, T, M, and C represent the orthorhombic, rhombohedral, tetragonal, monoclinic, and cubic phases, respectively.

competition between multiple structural phases. The phase diagram is readily reproducible in experiments and has been extensively studied since its initial depiction in 1971 by Jaffe *et al.* [4]. But relevant theoretical research is still lacking due to the higher computational precision requirements and structural complexity [46]. Here, the DP model allows us to perform DPMD simulations for different compositions at finite temperatures. We present the temperature phase diagrams for pure PZO and PTO in Figs. 4(a) and 4(b). They show that PZO transitions from the antiferroelectric orthorhombic (O) phase to the cubic (C) phase at 460 K, while PTO transitions from the ferroelectric tetragonal (T) phase to the cubic (C) phase at 530 K, consistent with the experiment works [47]. In Figs. 4(c) and 4(d), we plot the temperature phase diagram at $x = 0.5$. It is found that PZT successively exhibits four phases—rhombohedral (R), monoclinic (M), tetragonal (T), and cubic (C)—as the temperature rises. The presence of the monoclinic phase between the rhombohedral phase and tetragonal phase occurs at 370–470 K, which differs from the one reported in a recent work [36]. Their calculation results indicate a direct transition from the rhombohedral phase to the tetragonal phase without the bridged monoclinic phase. We assume the reason for the difference is that the universal model for perovskite oxides might lose the accuracy to describe minor details within certain systems. We also obtain the temperature-composition phase diagram over a whole range of compositions shown in Fig. 5. Five phases are found in this phase diagram, consistent with experiment. The

antiferroelectric orthorhombic phase is observed in the range $x = 0 - 0.08$, on the left of the blue line. As x increases, the ferroelectric rhombohedral phase with polarization along the [111] direction appears. Furthermore, when x becomes close to ~0.5, the most important region in the phase diagram,
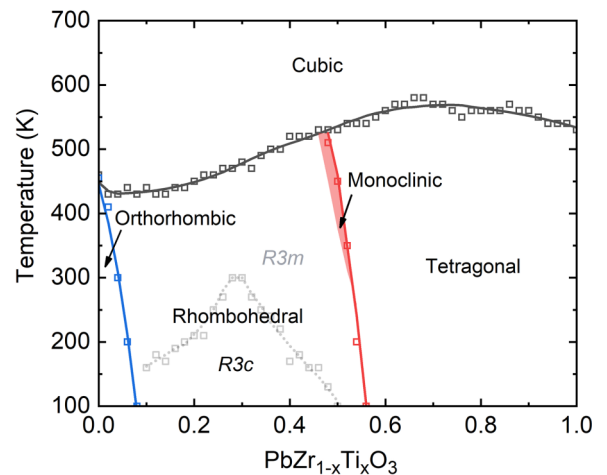
FIG. 5. DP-predicted temperature-composition phase diagram of PZT. Red line represents the MPB and the red shaded area represents the monoclinic phase near the MPB. The gray dashed line represents the artificially defined hypothetical boundary between the *R3m* and *R3c* structures.
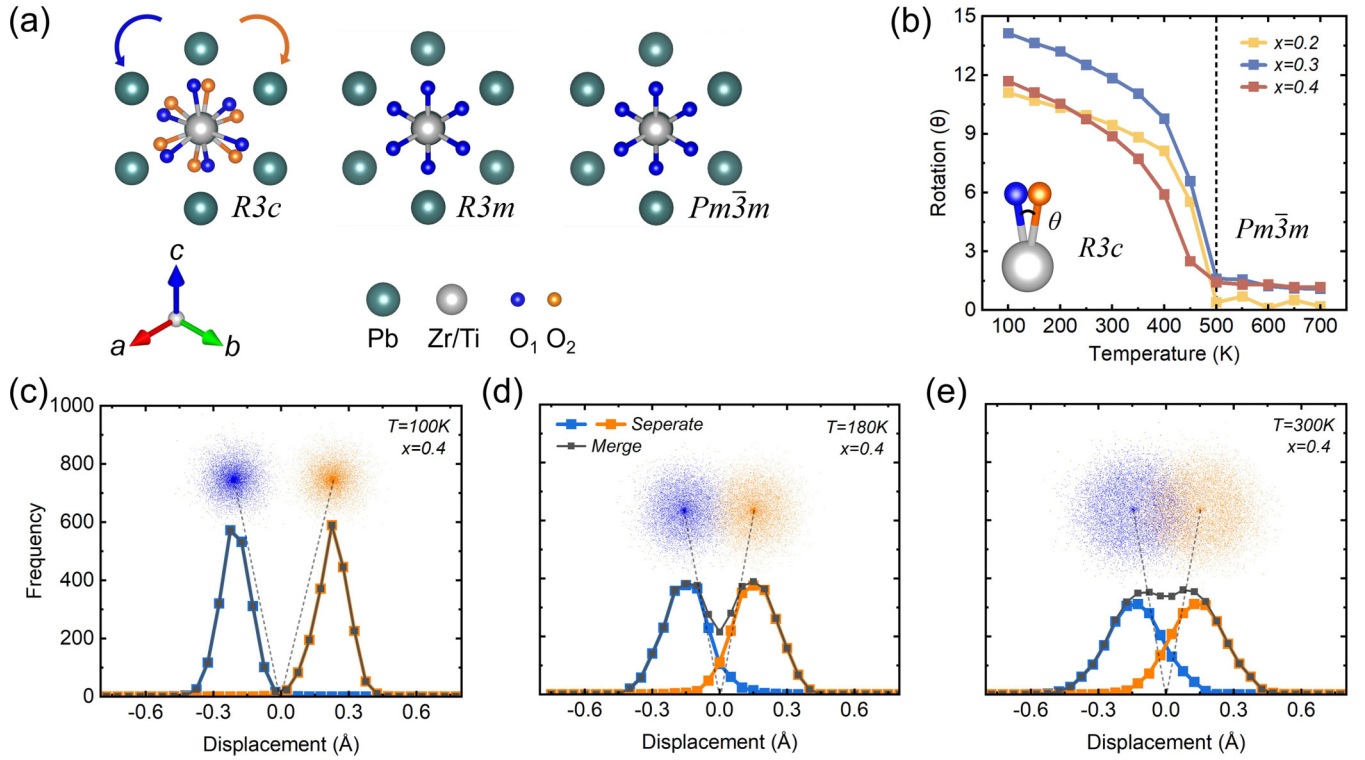
FIG. 6. (a) Crystal structures along the [111] direction in the $R3c$, $R3m$, and $Pm\bar{3}m$ symmetries. O1 and O2 represent the oxygen atoms in the neighboring octahedra with reverse tilting. (b) The angle variation between O1 and O2 as a function of temperature. When $x = 0.4$, the real-space distribution of O1 and O2 at (c) $T = 100$ K, (d) $T = 180$ K, and (e) $T = 300$ K.

called the MPB, appears, marked by the red line. On the right-hand side of the MPB, the most stable structure is a tetragonal phase with polarization along the [001] direction. Additionally, we find the monoclinic phase at the MPB, indicating the monoclinic phase is a bridge between the rhombohedral phase and the tetragonal phase, in agreement with previous experiments [48,49]. At high temperatures, the ferroelectric phases transform to paraelectric cubic phases in a whole range of compositions as shown in Fig. 5. Details of the $R3m$ and $R3c$ structures in the phase diagram will be discussed below. The results of the phase diagram agree with the previous experimental results [4]. However, The DP-predicted phase diagram suggests a slight decrease in ferroelectric-paraelectric transition temperature on the side close to PTO. Experimentally, the temperature monotonously increases with x. This issue also appeared in other DP research [36], and it does not affect the investigation of the MPB region.

According to the previous experiments, researchers generally believe that there exists a structure transition from $R3c$ to $R3m$ with increasing temperature in the rhombohedral phase region [50,51]. However, our calculated results indicate the absence of $R3m$ symmetry. The distinction between these two symmetries is depicted in Fig. 6(a): the $R3c$ symmetry can be characterized by the neighboring TiO$_6$ octahedra tilting with a small angle in the opposite directions along the [111] direction, whereas the TiO$_6$ octahedra do not tilt in $R3m$ symmetry. The periodically arranged oxygen atoms in the first and second octahedra are labeled as O1 (colored blue) and O2 (colored orange) along the [111] direction. We perform statistical analysis of the rotation angles θ between

O1 and O2 versus temperature for different values of x. The result in Fig. 6(b) shows that θ decreases to zero approximately only because they transform into cubic phase at high temperature directly, around 500 K, instead of transitioning to $R3m$.

To further demonstrate the stability of $R3c$ symmetry, we calculate the phonon spectrum of PbZr$_{0.75}$Ti$_{0.25}$O$_3$ in $R3c$ and $R3m$ symmetries, with a $2 \times 2 \times 2$ supercell. In Figs. 7(a) and 7(b), it is clear that imaginary frequencies appear at the L and Γ points, indicating $R3m$ structure has multiple lattice instability. With information on lattice vibrations, we can calculate the free energy of the system. The Gibbs free energy is a crucial thermodynamic quantity used to assess the stability of phases. In Fig. 7(c), we calculate the free energy of $R3m$ and $R3c$ symmetries depending on temperature (see Computational Methods). The result shows the free energy of PbZr$_{0.75}$Ti$_{0.25}$O$_3$ in $R3m$ symmetry is 5.13 meV/atom higher than that in the $R3c$ symmetry at 0 K. In the temperature range before transforming into the cubic phase (460 K), the free energy of $R3m$ symmetry is consistently higher than that of $R3c$ symmetry, showing no intersection point. We also quantitatively analyze the impact of configurational entropy. We supplement the calculation with the analytic equation $S_{\text{conf}} = -Nk_B[x\ln x + (1-x)\ln(1-x)]$ (see Computational Methods), where x represents the concentration of Ti. The results show it can only reduce the free energy of $R3m$ and $R3c$ at the same temperature by the same value. The curves of free energy still show no intersection point [see Fig. 7(c)]. Thus, configurational entropy does not have a qualitative impact on our results of $R3m$ and $R3c$ symmetry.
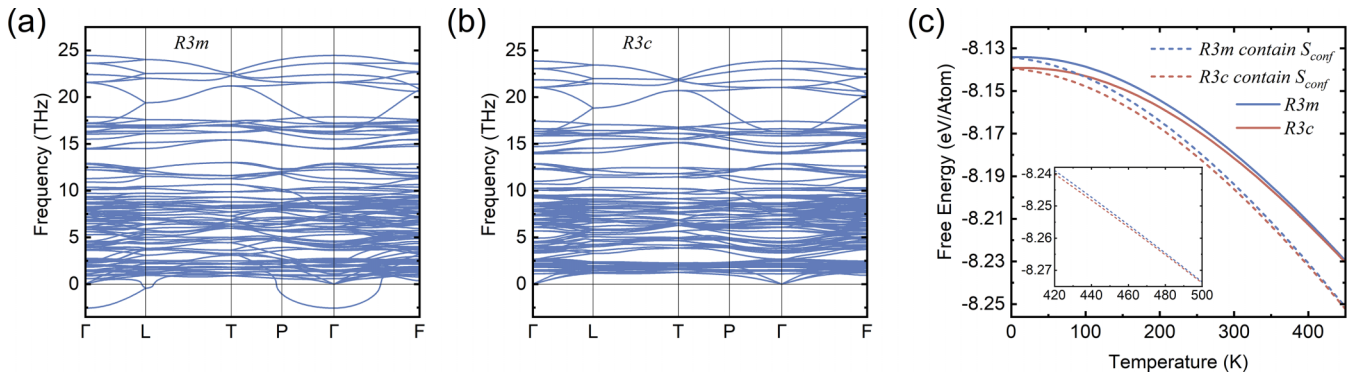
FIG. 7. The phonon spectrum of PbZr$_{0.75}$Ti$_{0.25}$O$_3$ in (a) *R3c* and (b) *R3m* symmetries, with a $2 \times 2 \times 2$ supercell. (c) Comparison of free energy of *R3m* and *R3c* symmetries, containing configurational entropy and not, respectively.

We assume the structure transition which was observed in the rhombohedral phase in experimental data is a result of the limitation of experimental measurements. The real-space distribution schematic diagram of O1 and O2 is provided in Figs. 6(c)–6(e). We performed a statistical analysis to determine the frequency of atom occurrence at various spatial positions. When O1 and O2 are counted separately, it is clear that O1 and O2 exhibit a Gaussian distribution at their respective positions. Considering that experimentally distinguishing between oxygen atoms in different octahedra is not feasible, we have combined O1 and O2 for statistical purposes. The results indicate that, with the increase of temperature, the two distribution peaks gradually merge into one single peak, corresponding to the inability to distinguish between O1 and O2 in real space. Therefore, some previous studies have suggested the presence of a structural transition from *R3c* to *R3m*, which actually does not occur. We artificially define that if the height of the saddle point exceeds the half height of the two sides peaks, it is "considered" to transfer to the structure in *R3m* symmetry. For example, as shown in Fig. 6(d), at $x = 0.4$ and $T = 180$ K, the merged peaks of O1 and O2 reach the "distinguishing limit." According to this criterion, we mark the gray dashed line in Fig. 5, fitting well with the previous studies [4].

C. High piezoelectric performance in MPB

The next issue is to determine the exact origin of high piezoelectricity at the MPB region. Piezoelectric materials exhibit a strain response under an electric field. The piezoelectric coefficient (d_{33}) can be characterized by the differential of strain over electric field. In Figs. 8(a) and 8(b), we plot the strain–electric field curves near the MPB region at 100 and 300 K. It clearly shows that the curves exhibit different behaviors with different x. Taking 100 K as an example, when $x \leqslant 0.50$, strain increases linearly with the electric field. When $0.5 < x \leqslant 0.56$, the strain exhibits three stages: linear, abrupt change, and linear. The abrupt change is due to the polarization rotation, and details will be discussed below. With increasing x, the electric field strength required for the abrupt change decreases. When $x > 0.56$, the relationship between strain and electric field reverts to being linear. We define $x = 0.56$ as the critical point at 100 K. As x exceeds this value, no sudden change occurs in strain. Similar behavior is observed at 300 K as well, with a different critical point occurring at $x = 0.52$. Based on the derivative of strain with respect to electric field with a range of $(0–1) \times 10^2$ kV/cm, we extract the piezoelectric coefficient d_{33} as shown in Fig. 8(c). (The detailed calculation content of d_{33} can be seen in Computational Methods.) Evidently, d_{33} experiences a significant
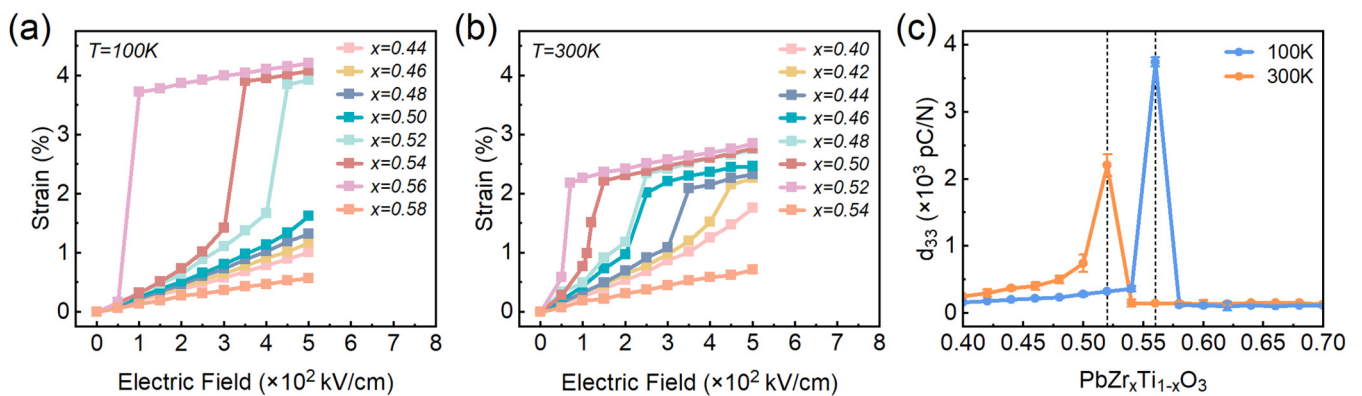
FIG. 8. Strain variation with electric field at (a) 100 K and (b) 300 K. Different colors represent distinct values of x. A higher slope indicates better piezoelectric performance. (c) The variation of d_{33} with respect to x at different temperatures. d_{33} reaches its maximum at $x = 0.56$, $T = 100$ K, and $x = 0.52$, $T = 300$ K. We add error bars by repeating calculations with five random disorder structures for each data point.
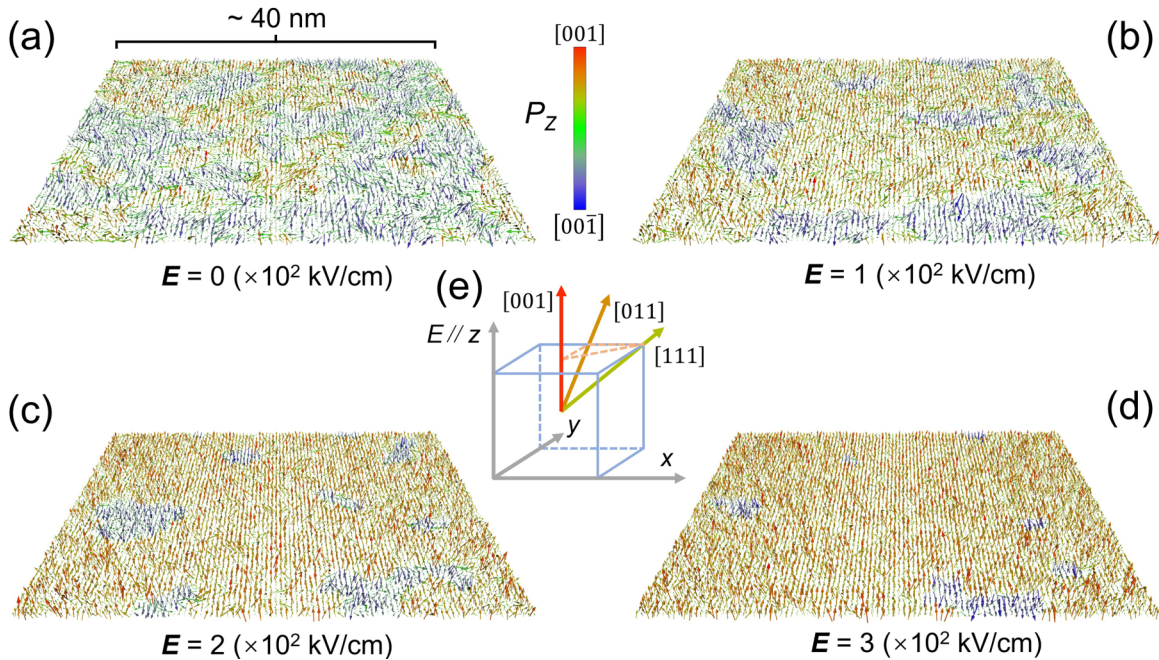
FIG. 9. Typical snapshots of dipole configurations of $PbZr_{0.5}Ti_{0.5}O_3$ with electric field (a) 0, (b) 1, (c) 2, and (d) 3×10^2 kV/cm, at 300 K. The color bar represents the polarization component along the z direction. Each arrow represents the local electric dipole vector within a pseudocubic unit cell. (e) Schematic diagram of polarization orientations for the rhombohedral phase along [111], the monoclinic phase along [011], and the tetragonal phase along [001].

increase to its maximum at the critical points, where $x = 0.56$, $T = 100$ K, and $x = 0.52$, $T = 300$ K. The trend of d_{33} changing with x aligns well with previous research [3]. The conclusion drawn is that critical points are highly temperature sensitive, with x decreasing as temperature increases. Its trajectory aligns closely with the red line in Fig. 5, corresponding to the MPB in the phase diagram. Thus, the MPB is indeed the region with the best piezoelectric performance. The DP-predicted d_{33} are larger than the experiment results [52]. We attribute this phenomenon to the order degree of Zr/Ti atomic arrangement. Extensive details will be elaborated in a future publication.

To unveil the microscale mechanisms behind the high piezoelectric properties in the MPB region, we plot the snapshots of electric dipole configurations with different electric field at $x = 0.5$, $T = 300$ K in Fig. 9. When the electric field is zero [see Fig. 9(a)], the dipoles exhibit a complex nanodomain structure with polarization orientations roughly along the eight directions, including [111] and its equivalent directions. As the electric field strength is increased to 1×10^2 kV/cm [see Fig. 9(b)], an increasing number of dipoles start to reorient toward the [001] direction, and nanodomains with polarization along [001] gradually grow larger. As the field increases to 2×10^2 kV/cm [see Fig. 9(c)], almost all dipoles align exclusively in the [001] direction, representing the polarization rotation tending toward saturation. The polarization rotation process corresponds to the abrupt change stage in the strain-electric field curve of Fig. 8(a), also corresponding to the phase transition from rhombohedral phase to tetragonal phase of PZT. Moreover, the intermediate transitional monoclinic phase observed in the phase diagram suggests that there is a metastable [011] orientation between the polarizations in the [111] and [001] directions, serving as a

bridge for the phase transition [12]. As the electric field further increase to 3×10^2 kV/cm [see Fig. 9(d)], dipoles aligning toward the [001] direction only increase in magnitude, corresponding to the linear stage on the curve. The process of polarization rotation leads to the high d_{33} value of 2263 pC/N at the MPB. We also plotted snapshots of pure PTO for comparison of piezoelectricity. As shown in Fig. 10, PTO exhibits a tetragonal phase with different polarization orientations, resulting in a simpler domain structure. Unlike at the MPB, the domain structure evolution shows minimal changes with the increasing electric field instead of polarization rotation. This corresponds to the strain–electric field curve that linearly ascends with a small slope. The calculated d_{33} is 471 pC/N, significantly lower than the result at the MPB.

To more intuitively and quantitatively observe the polarization characteristics, we statistically analyzed the frequency distribution on the displacement of B-site atoms relative to the oxygen octahedral center in the $PbZr_{0.5}Ti_{0.5}O_3$ and PTO domain structures (see Fig. 11). As shown in Fig. 11(a), when no external electric field is applied, the polarization component of $PbZr_{0.5}Ti_{0.5}O_3$ is isotropically distributed around zero, corresponding to the complex domain structure of various polarization orientations in Fig. 9(a). When the electric field increases to 3×10^2 kV/cm, the peak of the z component shifts significantly to the right, corresponding to the movement of B-site atoms toward the z direction. The distribution peaks of the x and y components become sharper [see Fig. 11(c)]. These results indicate that the vast majority of dipoles reorient to the [001], corresponding to Fig. 9(d), whereas the pure PTO exhibits no significant differences before and after the electric field is applied. In Figs. 11(b) and 11(d), dipoles only have a slight response to the electric field in the z direction. The same electric field is not sufficient
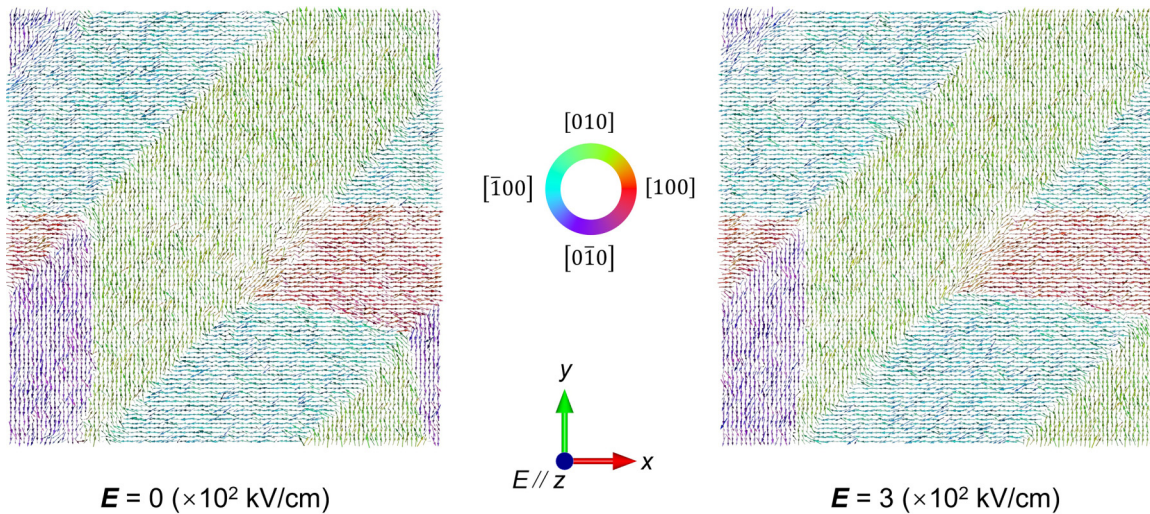
FIG. 10. Typical snapshots of dipole configurations of PTO with different electric field at 300 K. The colored circle represents the polarization orientation. Each arrow represents the local electric dipole vector within a pseudocubic unit cell. The domain structure exhibits a tiny response with the electric field.

to reorient the polarization direction of the domain to the z axis. This behavior is significantly different from the one of $PbZr_{0.5}Ti_{0.5}O_3$. Therefore, a small electric field can induce

the polarization rotation as x is close to the MPB, leading to a significant change in lattice constants, which explains the outstanding piezoelectricity of PZT at the MPB.
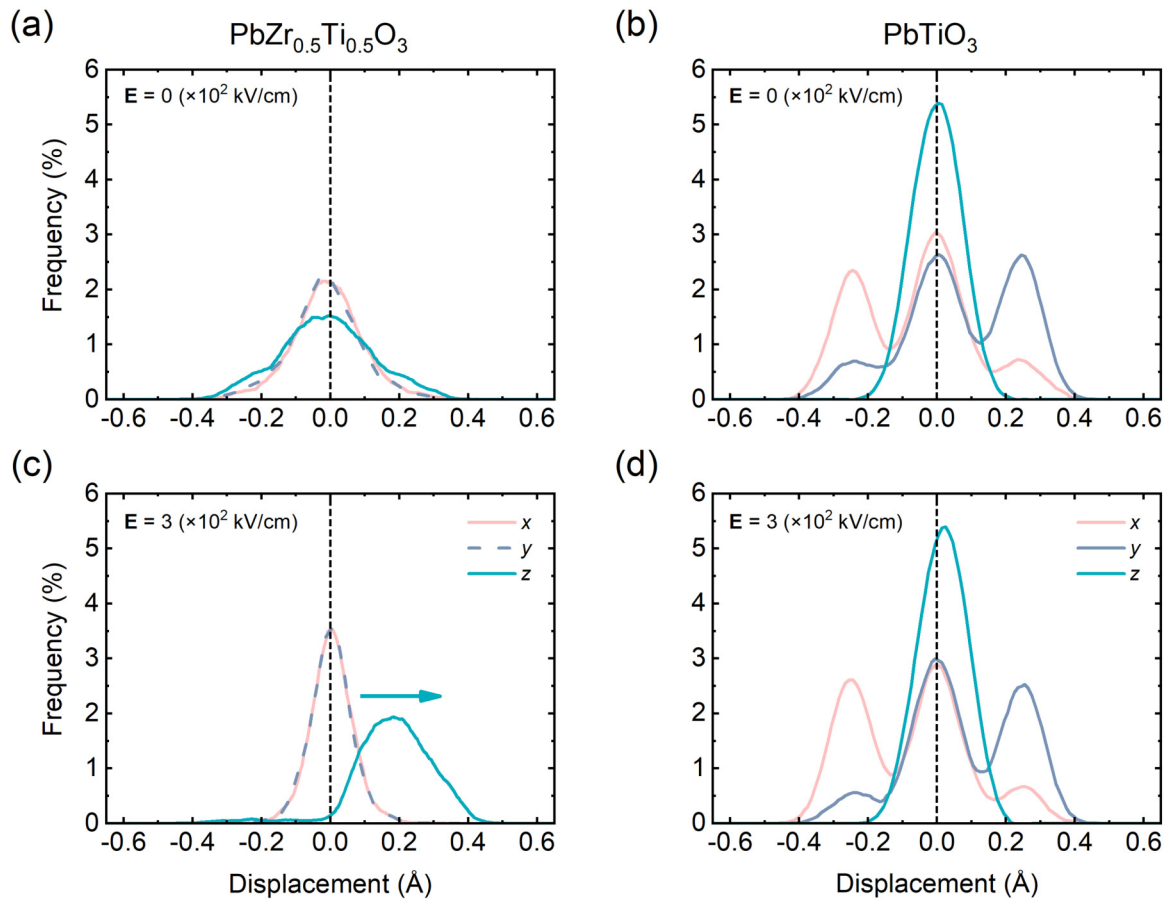
FIG. 11. Frequency distributions of B-site atoms relative to the oxygen octahedral center displacements at 300 K. We separately analyzed the structures under $\mathbf{E} = 0$ and 3×10^2 kV/cm, in both $PbZr_{0.5}Ti_{0.5}O_3$ and PTO.

IV. CONCLUSION

In summary, we develop the DP model based on the machine learning method to simulate the piezoelectric property and phase transition of PZT, particularly near the MPB. Initially, we reproduce the temperature-composition phase diagram of PZT by computational methods. More importantly, we observe the absence of the *R3m* symmetry in the rhombohedral phase, contrary to experiment. *R3m* and *R3c* symmetries are very similar, except for oxygen octahedral tilting along the [111] direction in *R3c*. We find that the rhombohedral phase maintains *R3c* symmetry with slight oxygen octahedral tilting the temperature is increased, instead of appearing as *R3m* symmetry. We believe the reason may be that oxygen octahedral tilting becomes too small to distinguish by experimental measurements. We extensively discuss the piezoelectric properties near the MPB. In contrast to the simple domain structure of pure PTO, PZT at the MPB exhibits a competition of complex ferroelectric nanodomain structures with different polarization orientations. This clarifies the critical role of electric-field-driven polarization rotation in the high-piezoelectricity phenomenon. Our work demonstrates that the DP model can accurately capture the kinetic and thermodynamic properties of complex solid solution domain structures at the atomic level, which is crucial for understanding the microscopic origins of piezoelectricity and exploring the realm of dielectric energy storage.

[1] K. Uchino, *Ferroelectric Devices* (CRC Press, Boca Raton, FL, 2018).

[2] N. Izyumskaya, Y.-I. Alivov, S.-J. Cho, H. Morkoç, H. Lee, and Y.-S. Kang, Processing, structure, properties, and applications of PZT thin films, Crit. Rev. Solid State Mater. Sci. **32**, 111 (2007).

[3] B. Jaffe, R. Roth, and S. Marzullo, Piezoelectric properties of lead zirconate-lead titanate solid-solution ceramics, J. Appl. Phys. **25**, 809 (1954).

[4] B. Jaffe, W. R. Cook, and H. L. Jaffe, *Piezoelectric Ceramics* (Academic Press, San Diego, CA, 1971).

[5] A.-B. M. Ibrahim, R. Murgan, M. Rahman, and J. Osman, Morphotropic phase boundary in ferroelectric materials, Ferroelectr.: Phys. Eff. 4 (2011).

[6] V. Isupov, Dielectric polarization of PbTiO₃-PbZrO₃ solid solutions, Sov. Phys. Solid State, USSR **12**, 1084 (1970).

[7] P. Ari-Gur and L. Benguigui, X-ray study of the PZT solid solutions near the morphotropic phase transition, Solid State Commun. **15**, 1077 (1974).

[8] P. Ari-Gur and L. Benguigui, Direct determination of the coexistence region in the solid solutions Pb(Zr$_x$Ti$_{1-x}$)O₃, J. Phys. D Appl. Phys. **8**, 1856 (1975).

[9] V. Isupov, Comments on the paper "X-ray study of the PZT solid solutions near the morphotropic phase transition", Solid State Commun. **17**, 1331 (1975).

[10] K. Kakegawa, J. Mohri, T. Takahashi, H. Yamamura, and S. Shirasaki, A compositional fluctuation and properties of Pb(Zr, Ti)O₃, Solid State Commun. **24**, 769 (1977).

[11] S. M. Gupta and D. Viehland, Tetragonal to rhombohedral transformation in the lead zirconium titanate lead magnesium niobate-lead titanate crystalline solution, J. Appl. Phys. **83**, 407 (1998).

[12] H. Fu and R. E. Cohen, Polarization rotation mechanism for ultrahigh electromechanical response in single-crystal piezoelectrics, Nature (London) **403**, 281 (2000).

[13] R. Guo, L. Cross, S. Park, B. Noheda, D. Cox, and G. Shirane, Origin of the high piezoelectric response in PbZr$_{1-x}$Ti$_x$O₃, Phys. Rev. Lett. **84**, 5423 (2000).

[14] L. Bellaiche and D. Vanderbilt, Intrinsic piezoelectric response in perovskite alloys: PMN-PT versus PZT, Phys. Rev. Lett. **83**, 1347 (1999).

[15] M. Ahart, M. Somayazulu, R. Cohen, P. Ganesh, P. Dera, H.-k. Mao, R. J. Hemley, Y. Ren, P. Liermann, and Z. Wu, Origin of morphotropic phase boundaries in ferroelectrics, Nature (London) **451**, 545 (2008).

[16] J. Frantti, J. Lappalainen, S. Eriksson, S. Ivanov, V. Lantto, S. Nishio, M. Kakihana, and H. Rundlöf, Neutron diffraction studies of Pb(Zr$_x$Ti$_{1-x}$)O₃ ceramics, Ferroelectrics **261**, 193 (2001).

[17] J. Frantti, S. Ivanov, J. Lappalainen, S. Eriksson, V. Lantto, S. Nishio, M. Kakihana, and H. Rundlöf, Local and average structure of lead titanate based ceramics, Ferroelectrics **266**, 409 (2002).

[18] J. Frantti, Y. Fujioka, and R. Nieminen, Pressure-induced phase transitions in PbTiO₃: A query for the polarization rotation theory, J. Phys. Chem. B **111**, 4287 (2007).

[19] J. Frantti, Notes of the recent structural studies on lead zirconate titanate, J. Phys. Chem. B **112**, 6521 (2008).

[20] J. Li, R. Rogan, E. Üstündag, and K. Bhattacharya, Domain switching in polycrystalline ferroelectric ceramics, Nat. Mater. **4**, 776 (2005).

[21] T. Asada and Y. Koyama, Ferroelectric domain structures around the morphotropic phase boundary of the piezoelectric material PbZr$_{1-x}$Ti$_x$O₃, Phys. Rev. B **75**, 214111 (2007).

[22] Y. Jin, Y. U. Wang, A. G. Khachaturyan, J. Li, and D. Viehland, Conformal miniaturization of domains with low domain-wall energy: Monoclinic ferroelectric states near the morphotropic phase boundaries, Phys. Rev. Lett. **91**, 197601 (2003).

[23] K. A. Schönau, L. A. Schmitt, M. Knapp, H. Fuess, R.-A. Eichel, H. Kungl, and M. J. Hoffmann, Nanodomain structure

of Pb[Zr$_{1-x}$Ti$_x$]O$_3$ at its morphotropic phase boundary: Investigations from local to average structure, Phys. Rev. B **75**, 184117 (2007).

[24] W.-F. Rao and Y. U. Wang, Microstructures of coherent phase decomposition near morphotropic phase boundary in lead zirconate titanate, Appl. Phys. Lett. **91**, 052901 (2007).

[25] K. Yan, S. Ren, M. Fang, and X. Ren, Crucial role of octahedral untilting *R3m/P4mm* morphotropic phase boundary in highly piezoelectric perovskite oxide, Acta Mater. **134**, 195 (2017).

[26] R. He, H. Wu, L. Zhang, X. Wang, F. Fu, S. Liu, and Z. Zhong, Structural phase transitions in SrTiO$_3$ from deep potential molecular dynamics, Phys. Rev. B **105**, 064104 (2022).

[27] H. Wu, R. He, Y. Lu, and Z. Zhong, Large-scale atomistic simulation of quantum effects in SrTiO$_3$ from first principles, Phys. Rev. B **106**, 224102 (2022).

[28] R. He, H. Xu, P. Yang, K. Chang, H. Wang, and Z. Zhong, Ferroelastic twin-wall-mediated ferroelectriclike behavior and bulk photovoltaic effect in SrTiO$_3$, Phys. Rev. Lett. **132**, 176801 (2024).

[29] R. He, B. Zhang, H. Wang, L. Li, T. Ping, G. Bauer, and Z. Zhong, Ultrafast switching dynamics of the ferroelectric order in stacking-engineered ferroelectrics, Acta Mater. **262**, 119416 (2024).

[30] Y. Zhang, H. Wang, W. Chen, J. Zeng, L. Zhang, H. Wang, and E. Weinan, DP-GEN: A concurrent learning platform for the generation of reliable deep learning based potential energy models, Comput. Phys. Commun. **253**, 107206 (2020).

[31] T. Wen, L. Zhang, H. Wang, E. Weinan, and D. J. Srolovitz, Deep potentials for materials science, Mater. Futures **1**, 022601 (2022).

[32] H. Wang, L. Zhang, J. Han, and E. Weinan, DeePMD-kit: A deep learning package for many-body potential energy representation and molecular dynamics, Comput. Phys. Commun. **228**, 178 (2018).

[33] D. Lu, W. Jiang, Y. Chen, L. Zhang, W. Jia, H. Wang, and M. Chen, DP compress: A model compression scheme for generating efficient deep potential models, J. Chem. Theory Comput. **18**, 5559 (2022).

[34] J. Wu, Y. Zhang, L. Zhang, and S. Liu, Deep learning of accurate force field of ferroelectric HfO$_2$, Phys. Rev. B **103**, 024108 (2021).

[35] R. He, H. Wu, Y. Lu, and Z. Zhong, Origin of negative thermal expansion and pressure-induced amorphization in zirconium tungstate from a machine-learning potential, Phys. Rev. B **106**, 174101 (2022).

[36] J. Wu, J. Yang, Y.-J. Liu, D. Zhang, Y. Yang, Y. Zhang, L. Zhang, and S. Liu, Universal interatomic potential for perovskite oxides, Phys. Rev. B **108**, L180104 (2023).

[37] L. Zhang, H. Wang, M. C. Muniz, A. Z. Panagiotopoulos, and R. Car, A deep potential model with long-range electrostatic interactions, J. Chem. Phys. **156**, 124107 (2022).

[38] G. Kresse and J. Furthmüller, Efficient iterative schemes for *ab initio* total-energy calculations using a plane-wave basis set, Phys. Rev. B **54**, 11169 (1996).

[39] G. Kresse and J. Furthmüller, Efficiency of *ab-initio* total energy calculations for metals and semiconductors using a plane-wave basis set, Comput. Mater. Sci. **6**, 15 (1996).

[40] J. P. Perdew, K. Burke, and M. Ernzerhof, Generalized gradient approximation made simple, Phys. Rev. Lett. **77**, 3865 (1996).

[41] A. Togo, First-principles phonon calculations with PHONOPY and PHONO3PY, J. Phys. Soc. Jpn. **92**, 012001 (2023).

[42] A. Togo, L. Chaput, T. Tadano, and I. Tanaka, Implementation strategies in PHONOPY and PHONO3PY, J. Phys. Condens. Matter **35**, 353001 (2023).

[43] S. Plimpton, Fast parallel algorithms for short-range molecular dynamics, J. Comput. Phys. **117**, 1 (1995).

[44] A. P. Thompson, H. M. Aktulga, R. Berger, D. S. Bolintineanu, W. M. Brown, P. S. Crozier, P. J. in't Veld, A. Kohlmeyer, S. G. Moore, and T. D. Nguyen, LAMMPS- a flexible simulation tool for particle-based materials modeling at the atomic, meso, and continuum scales, Comput. Phys. Commun. **271**, 108171 (2022).

[45] W. Zhong, R. King-Smith, and D. Vanderbilt, Giant LO-TO splittings in perovskite ferroelectrics, Phys. Rev. Lett. **72**, 3618 (1994).

[46] O. Gindele, A. Kimmel, M. G. Cain, and D. Duffy, Shell model force field for lead zirconate titanate Pb(Zr$_{1-x}$Ti$_x$)O$_3$, J. Phys. Chem. C **119**, 17784 (2015).

[47] M. J. Haun, E. Furman, S. Jang, H. McKinstry, and L. Cross, Thermodynamic theory of PbTiO$_3$, J. Appl. Phys. **62**, 3331 (1987).

[48] B. Noheda, D. Cox, G. Shirane, J. Gonzalo, L. Cross, and S. Park, A monoclinic ferroelectric phase in the Pb(Zr$_{1-x}$Ti$_x$)O$_3$ solid solution, Appl. Phys. Lett. **74**, 2059 (1999).

[49] B. Noheda, J. Gonzalo, L. Cross, R. Guo, S.-E. Park, D. Cox, and G. Shirane, Tetragonal-to-monoclinic phase transition in a ferroelectric perovskite: The structure of PbZr$_{0.52}$Ti$_{0.48}$O$_3$, Phys. Rev. B **61**, 8687 (2000).

[50] C. Michel, J.-M. Moreau, G. D. Achenbach, R. Gerson, and W. J. James, Atomic structures of two rhombohedral ferroelectric phases in the Pb(Zr, Ti)O$_3$ solid solution series, Solid State Commun. **7**, 865 (1969).

[51] R. Eitel and C. Randall, Octahedral tilt-suppression of ferroelectric domain wall dynamics and the associated piezoelectric activity in Pb(Zr, Ti)O$_3$, Phys. Rev. B **75**, 094106 (2007).

[52] D. Damjanovic, in *Piezoelectric and Acoustic Materials for Transducer Applications* (Springer, Berlin, 2008), pp. 59–79.